Multi-Pinhole X-ray Fluorescence Imaging System on Pixelated Detector: A Monte Carlo Study

Taeyun Kim [a], Mingi Eom [a], Sung-Joon Ye [a,b,c,d*]
[a]*Department of Applied Bioengineering, Graduate School of Convergence Science and Technology, Seoul National University, Seoul, 08826, Republic of Korea*
[b]*Research Institute for Convergence Science, Seoul National University, Seoul, 08826, Republic of Korea*
[c]*Advanced Institute of Convergence Technology, Seoul National University, Suwon, 16229, Republic of Korea*
[d]*Biomedical Research Institute, Seoul National University Hospital, Seoul, 03080, Republic of Korea*

[*]*Corresponding author: sye@snu.ac.kr*

1. Introduction

X-ray fluorescence (XRF) imaging holds considerable promise as a molecular imaging modality, enabling the precise assessment of the biodistribution of metal nanoparticles (MNPs), which have garnered attention as nanomedicine materials due to their unique properties [1, 2]. Among various MNPs (e.g., gadolinium, hafnium, iron, silver, and gold), gold nanoparticles (GNPs) are particularly widely used because of their relatively good biocompatibility. The major challenge of the current XRF imaging modality is improving the system sensitivity (i.e., detection limit). This can be effectively addressed through the introduction of a high-energy resolution detector or the implementation of a multi-pinhole collimator to improve detection efficiency. In this study, a Monte Carlo (MC) model of a pixelated detector-based multi-pinhole XRF imaging system was developed to quantitatively evaluate the improvement of system sensitivity.

2. Materials and Methods

2.1 Monte Carlo simulation

A pixelated detector-based multi-pinhole XRF imaging system was modeled using MCNP6 (version 6.2.0). As shown in Fig. 1, a small animal-sized polymethyl methacrylate (PMMA) phantom (1 cm in diameter, 1 cm in length) was placed in the center of the two pinhole collimators. Within the PMMA phantom center, four columns of 0.3 cm in diameter and 0.6 cm in height were inserted. These columns were filled with GNP-containing solutions of different concentrations (0.125, 0.25, 0.5, and 1 wt%). The two lead pinhole collimators have single- or multi-pinhole (5 pinholes). The diameter of each pinhole was 1 mm, the distance between the pinholes was 7.5 mm, and the thickness was 9 mm.

The pixelated detector was made of 160 × 160 cadmium telluride (CdTe) crystal and had a pixel pitch of 250 μm. The energy spectrum in each CdTe crystal was obtained using the F8 tally. To reduce computational time, detectors were placed on both sides of the incident X-ray at 90°. To shield unwanted photons from incident on the detector, a cylindrically shaped 5 mm thick tungsten collimator was attached to the detector. For the generation of K-shell XRF photons from gold, a 140 kV polychromatic X-ray beam was utilized, which was filtered using 1.5 mm Al, 0.25 mm Cu, and 0.75 mm Sn. The energy spectrum used in this study was extracted from SpekCalc.

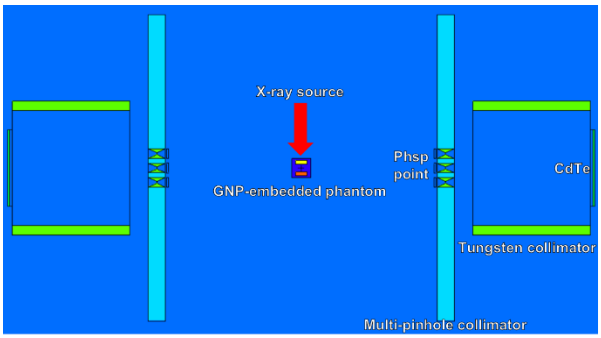

Fig. 1. A pixelated detector-based multi-pinhole X-ray fluorescence imaging system modeled using MCNP6.

3. Results and Discussion

3.1 X-ray fluorescence image

Fig. 2 shows a multi-pinhole XRF image. Five pinhole projections were generated by a multi-pinhole collimator. In a single-pinhole XRF image, only the central pinhole projection was generated. Notably, the four GNP columns were distinctly discernible across all generated pinhole projections.

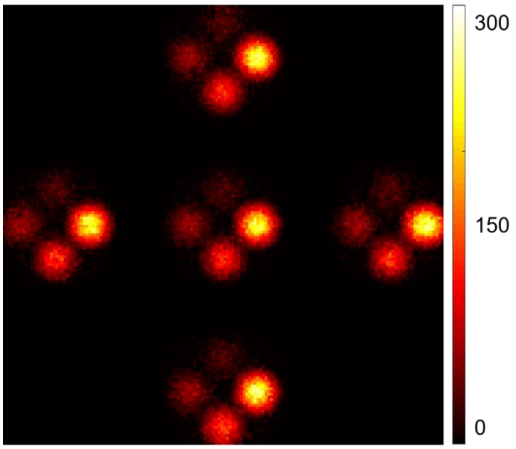

Fig. 2. Multi-pinhole XRF image of a PMMA phantom with four GNP columns.

To quantitatively analyze single- and multi-pinhole XRF images, a comparative evaluation was conducted between the central pinhole projection and the aggregate of all pinhole projections. Compared to the single-pinhole XRF image, the XRF photon count of the multi-pinhole XRF image was about 4.9 times greater. As shown in Fig. 3, there was also an improvement in the contrast-to-noise ratio (CNR). At a concentration of 0.125 wt% GNP, the single-pinhole XRF image had a CNR of 9, while the multi-pinhole XRF image demonstrated a significantly improved CNR of 17. According to the Rose criterion for CNR (CNR > 5), the detection limit for the single-pinhole XRF image was determined to be 0.06 wt%, whereas the multi-pinhole XRF image displayed a lowered detection limit of 0.03 wt%.

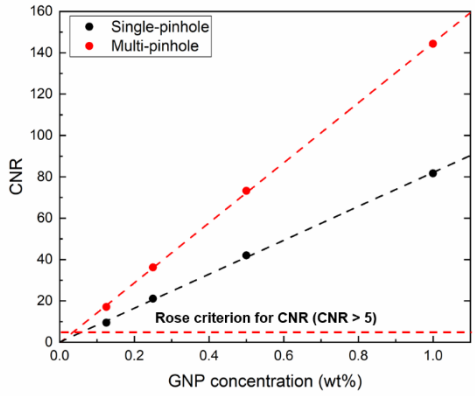

Fig. 3. CNR of the single- and multi-pinhole XRF image for each GNP concentration.

4. Conclusions

This study aimed to enhance the detection limit of the XRF imaging system by implementing a high-energy resolution pixelated detector and a multi-pinhole collimator using MCNP6. Using a high-energy resolution pixelated detector has resulted in significant improvements in both energy and spatial resolutions compared to conventional pixelated detectors. Consequently, this improvement can lower the detection limit of the XRF imaging system. Furthermore, the feasibility of the multi-pinhole collimator was evaluated, which demonstrated the capability to further reduce the detection limit by increasing detection efficiency. In the future, we will enhance the validity of the simulation by conducting comparisons with other MC simulation codes such as Geant4 [3]. Additionally, we will overcome the limitations of XRF imaging, which provides only functional information, by incorporating computed tomography, which provides anatomical information [4].

Acknowledgements

This work was supported by the National Research Foundation of Korea (NRF) grant funded by the Korea government (MSIT) (No. RS-2023-00237149).

REFERENCES

[1] T. Kim, W. Lee, M. Jeon, H. Kim, M. Eom, S. Jung, H.J. Im, and S.J. Ye, Dual imaging modality of fluorescence and transmission X-rays for gold nanoparticle-injected living mice, Med. Phys., Vol. 50, p. 529–539, 2023.
[2] S. Jung, T. Kim, W. Lee, H. Kim, H.S. Kim, H.J. Im, and S.J. Ye, Dynamic in vivo X-ray fluorescence imaging of gold in living mice exposed to gold nanoparticles, IEEE Trans. Med. Imaging., Vol. 39, p. 526–533, 2019.
[3] M. Eom, S. Youn, and S.J. Ye, Monte Carlo-based identification of electron and proton edges for calibration of miniaturized tissue equivalent proportional counter, Nucl. Eng. Technol., Vol. 55, p. 4167–4172, 2023.
[4] T. Kim, J. Lee, G.M. Sun, B.G. Park, H.J. Park, D.S. Choi, and S.J. Ye, Comparison of X-ray computed tomography and magnetic resonance imaging to detect pest-infested fruits: A pilot study, Nucl. Eng. Technol., Vol. 54, p. 514–522, 2022.